

Asymmetric three-dimensional topography over mantle plumes

Evgueni Burov^{1,2} & Taras Gerya³

The role of mantle–lithosphere interactions in shaping surface topography has long been debated^{1–3}. In general^{3,4}, it is supposed that mantle plumes and vertical mantle flows result in axisymmetric, long-wavelength topography, which strongly differs from the generally asymmetric short-wavelength topography created by intraplate tectonic forces. However, identification of mantle-induced topography is difficult³, especially in the continents⁵. It can be argued therefore that complex brittle–ductile rheology and stratification of the continental lithosphere result in short-wavelength modulation and localization of deformation induced by mantle flow⁶. This deformation should also be affected by far-field stresses and, hence, interplay with the ‘tectonic’ topography (for example, in the ‘active/passive’ rifting scenario^{7,8}). Testing these ideas requires fully coupled three-dimensional numerical modelling of mantle–lithosphere interactions, which so far has not been possible owing to the conceptual and technical limitations of earlier approaches. Here we present new, ultra-high-resolution, three-dimensional numerical experiments on topography over mantle plumes, incorporating a weakly pre-stressed (ultra-slow spreading), rheologically realistic lithosphere. The results show complex surface evolution, which is very different from the smooth, radially symmetric patterns usually assumed as the canonical surface signature of mantle upwellings⁹. In particular, the topography exhibits strongly asymmetric, small-scale, three-dimensional features, which include narrow and wide rifts, flexural flank uplifts and fault structures. This suggests a dominant role for continental rheological structure and intra-plate stresses in controlling dynamic topography, mantle–lithosphere interactions, and continental break-up processes above mantle plumes.

The question of the spatial scales at which surface topography is affected by mantle–lithosphere interactions rather than by plate-scale processes has attracted attention^{1–3,5–10} owing to its key importance for understanding the Earth’s tectonic, magmatic and seismic activity^{4,8}. This problem becomes crucial specifically in the light of current debates concerning the existence and impact of mantle plumes¹¹, the significance of the LAB (lithosphere–asthenosphere boundary), large-scale mantle–lithosphere instabilities¹² and lithosphere rheology¹³, and the mechanisms of continental rifting and breakup¹⁴. Of particular interest is the asymmetric or complex surface topography in regions where plate mechanics might influence mantle dynamics, such as the East African^{2,8,14,15}, Tanzanian^{8,14,15}, Red Sea^{8,14} and Dead Sea rift systems^{8,14}, the Pannonian–Carpathian system¹⁵, the Basin and Range province¹⁴, the Rio Grande rift and the Colorado plateau¹⁴, the Iranian and Tibetan plateaus¹⁴, the Yellowstone hotspot¹⁵, and some cratons^{15,16}. Mantle–lithosphere interactions have important consequences for tectonic evolution and for long-term climate change. For example, Archaean metallogenic ‘crises’ (sharp accelerations of metallogenic production) at the boundaries of the West African and Australian cratons and formation of volcanic traps coincide with plume events^{15–17} that have also played an important role in continental crustal accretion¹⁸ and in key geodynamic and environmental processes; and Siberian Traps magmatism is behind the greenhouse-gas emissions that led to global climate catastrophe and mass extinction of 80% of living species at the end of the Permian¹⁷.

The observation-based contribution of mantle flow to surface topography, dubbed ‘dynamic topography’³, is commonly evaluated by filtering out short-wavelength components ($\lambda < 1,000$ km) and by stripping local isostatic components of the observed topography and gravity and geoid fields². The remaining long-wavelength ($\lambda > 1,000$ km) undulations with amplitudes of the order of several hundred metres are regarded as an imprint of mantle flow. Such undulations are however difficult to separate from contributions due to heterogeneities in lithospheric structure, surface erosion and, in some cases, tectonic processes. Mantle flow is only hinted at by other observations such as gravity, seismic tomography, seismic anisotropy patterns (SKS orientations) or tectonic strain orientations^{2,3,10,19–23}. For instance, seismic tomography, which has been used to characterize mantle flow, does not always reveal features such as rising mantle plumes and sinking lithospheric slabs¹⁹. As a consequence, attempts to link mantle flow with surface dynamics often yield ambiguous results^{3,9}. These complications have triggered debates on the existence of mantle plumes^{11,19,21}, partitioning between mantle and tectonically driven processes^{6,7,9,13–15} and other questions such as the significance of dynamic topography^{9,20}. These disputes are fuelled, in particular, by the fact that axisymmetric dome uplifts expected above mantle upwellings^{1,6} are not unambiguously distinguished in the areas showing other (for example, tomographic, thermal, geochemical) evidence for mantle upwellings⁵: such areas include major recognized hotspots such as the African Superplume^{1,2}, Hawaii^{24,25}, and the ‘Afar Triangle’–Red Sea zone^{26,27}.

Surface impact of mantle–lithosphere interactions is usually predicted from three-dimensional (3D) numerical models of mantle dynamics^{2,9,10}. However, the existing models^{2,9,10} are designed to reproduce mantle flow and not surface deformation, as they: (1) do not compute surface topography (estimated *post hoc* from isostatic assumptions, Fig. 1a); (2) imply single-layer viscous stagnant lithosphere; and (3) have low spatial resolution, insufficient to resolve small-scale deformation and rheological stratification¹³.

High-resolution two-dimensional (2D) models^{6,15,28,29} of rheologically stratified lithosphere that are free of these limitations predict short-wavelength topography marked by closely spaced fault patterns and multi-harmonic tectonic-scale features with $\lambda \approx 30$ –100, 150–350 and 400–500 km. The reason for this is that thick rheologically stratified lithosphere acts to dampen and modulate the mantle flow ‘signal’ (Fig. 1). This is because the lower continental crust typically represents a low-viscosity 10–20-km-thick ductile channel^{6,13} that mechanically separates crust from mantle and absorbs undulations of crust–mantle interface (Moho) induced by mantle flow (Fig. 1). As a consequence, mantle flow stresses acting at the LAB are attenuated or re-focused, resulting in short-wavelength tensional/compressional instabilities in competent rheological layers constituting lithosphere. The actual wavelengths are controlled by the thicknesses of these layers and do not depend on the wavelength of mantle upwellings²⁹.

The 2D models provide little information, however, on 3D features of Earth’s surface topography. This is despite the fact that axisymmetric mantle upwellings or downwellings would be expected to produce axisymmetric radial topography and gravity, which are therefore searched-for in

¹Sorbonne Universités, UPMC Université Paris 06, UMR 7193, Institut des Sciences de la Terre Paris (ISTeP), F-75005 Paris, France. ²CNRS, UMR 7193, Institut des Sciences de la Terre Paris (ISTeP), F-75005 Paris, France. ³ETH, 8092 Zürich, Switzerland.

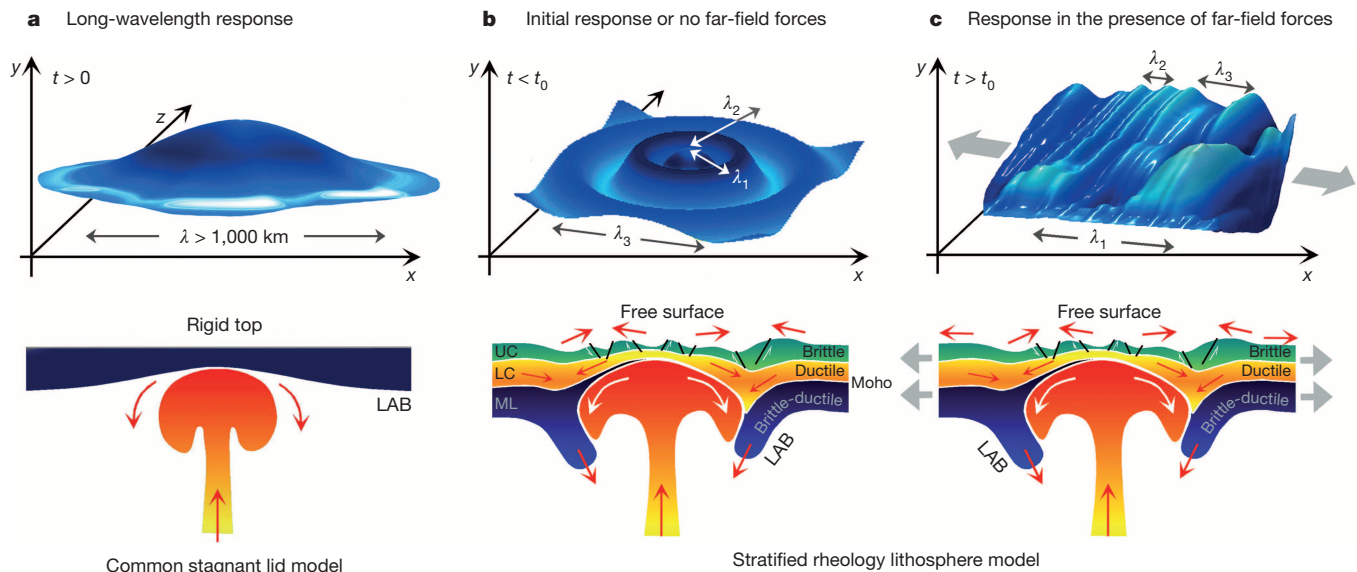


Figure 1 | Mantle-lithosphere interactions and topography. Evaluation of deformation of the Earth's surface caused by mantle flow (dynamic topography³) is commonly not straightforward and is based on additional assumptions; here we show surface topography (top row) and corresponding conceptual models (bottom row). In the conventional^{1,3,9} view (a), mantle upwellings can produce only long-wavelength ($\lambda > 1,000$ km) axisymmetric domes at the surface; in the corresponding models, the lithosphere commonly represents a passive flat-top viscous stagnant lid^{2,9,10} and the topography is computed from mantle flow patterns assuming local isostasy¹. Our approach (b, c) considers instead free-surface response of rheologically stratified

brittle-ductile lithosphere that may exhibit several short-wavelength harmonics^{6,29}, whereas long-wavelength deformation is dampened in the ductile lower crust (LC). The actual surface wavelengths λ_i (for example, $\lambda_1 \approx 30\text{--}50$, $\lambda_2 \approx 100\text{--}150$, $\lambda_3 \approx 250\text{--}350$ km) are controlled by thicknesses of strong upper crustal (UC), lower crustal (LC) and mantle-lithosphere (ML) layers⁶. The initial topography (b) may become strongly asymmetric after some short time t_0 in the case of even very weak far-field tectonic stresses that trigger anisotropic strain localizations (c). In the bottom row, red arrows and white arrows indicate direction of surface and subsurface movements. Black lines indicate faults, and white half-arrows indicate direction of movements on the fault interfaces.

spectral studies attempting to identify dynamic topography^{5,15} (Fig. 1). Yet, in the presence of a directional far stress/strain field, mantle flow may trigger development of non-axisymmetric features that are controlled by far-field stress/strain orientation and strain-localizing properties of the pre-existing lithosphere⁸ (Methods, Fig. 1).

These considerations suggest a need for a novel, tectonically realistic 3D modelling approach that encompasses large horizontal scales ($>1,000$ km \times $1,000$ km), the entire 650-km-deep upper mantle, and offers 'lithospheric-grade' numerical resolution ($\sim 2 \times 2 \times 2$ km) in order to handle rheological stratification and localized deformation²⁹. This implies unprecedented numerical efforts, huge mesh dimensions comprising several hundred million elements ($\sim 500^3$), and billions of moving rock markers, compared to the previous models that could handle only 10 times smaller arrays. To meet this challenge, we have designed an ultra-high-resolution model based on an optimized staggered grid/particle-in-cell method³⁰ (Methods). Several sets of 3D experiments exploring different geodynamic settings have been performed, totalling 10^6 hours (~ 114 years) of nodal processing time on the supercomputers of ETH and UPMC.

To reduce the tested parameter range, we conducted a series of fast 2D high-resolution parametric experiments^{6,15,29} (Methods, Extended Data Figs 1–4). The retained reference model considers a 200-km-wide plume impinging on the base of a 150-km-thick, 250-Myr-old lithosphere²⁹. We then conducted a set of 3D experiments for different far-field tectonic boundary conditions: (1) no far-field forces; (2) unidirectional pure shear extensional forcing; (3) bi-directional pure shear forcing; and (4) combined pure and simple shear forcing. The lateral boundary conditions correspond to ultra-slow velocities applied at model sides (3 mm yr^{-1} , typical for pre-breakup continental rifts affected by mantle upwellings, such as the Rio Grande and East African rifts¹⁴), so that the associated intra-plate stresses are very low—insufficient on their own to produce significant large-scale deformation (for example, passive rifting) during the time of plume impingement.

Figure 2 illustrates two end-member scenarios: ultra-slow stretching of a continental lithosphere in the absence of active mantle upwelling;

and active mantle plume upwelling impinging on a stress-free lithosphere. In the first case (Fig. 2a), ultra-slow tectonic stretching produces patterns of distributed small-offset parallel faults, in which the fault spacing (30–50 km) is controlled by the thickness of the upper-crustal brittle layer. These faults are distributed over 1,000-km scales, without focusing in any particular zone. In the second scenario (Fig. 2b), surface deformation is radially axisymmetric, with periodic multi-harmonic short-wavelength radial undulations ($\lambda \approx 30\text{--}250$ km, Fig. 2b, Extended Data Fig. 5). This result is consistent with rheologically realistic 2D models^{6,15,29} (Extended Data Figs 1–4), and (expectedly) disagrees with conventional 3D models^{9,10} ($\lambda > 1,000$ km). We note radial undulations at the bottom (LAB) of the lithosphere, with $\lambda \approx 200\text{--}250$ km, and shorter-wavelength ($\lambda \approx 30\text{--}100$ km) surface and crustal deformation (Fig. 2, Extended Data Fig. 5). Vertical motions in the crust and lithosphere that overlie the plume change with time. The surface shows a sequence of events as follows: (1) a short (<0.25 Myr) dynamic uplift; (2) a large subsidence, which is first caused by mechanical erosion (thinning) of the LAB by mantle flow above the upwelling plume, and then amplified by gravitational down-warping of the LAB caused by fast Rayleigh–Taylor instability in cold dense mantle lithosphere^{6,12}; (3) a surface uplift (at $\sim 0.5\text{--}1.0$ Myr) resulting from buoyancy and the dynamic push of the plume; and (4) a subsidence in the middle of the uplifted zone due to continuing interplay between plume and lithosphere mantle. The uplift/subsidence events alternate over several Myr as plume ponds at the LAB. Small initial radial crustal cracks (not distinguishable in Fig. 2b) vanish after ~ 0.25 Myr.

The predictions from the above 'end-member' cases depart strongly from those observed in our next experiment, which considers the mixed scenario of 'active/passive rifting'⁸, in which the lithosphere is submitted to ultra-slow far-field extension and simultaneously impinged upon by an upwelling mantle plume (Figs 3, 4, Extended Data Fig. 6). The initial radial uplift patterns disappear within the first 0.5 Myr, and a series of linear localized sub-parallel normal faults form in the direction normal to the direction of extension. When the plume impacts the base of the lithosphere, the lithosphere begins to thin in a single direction that is

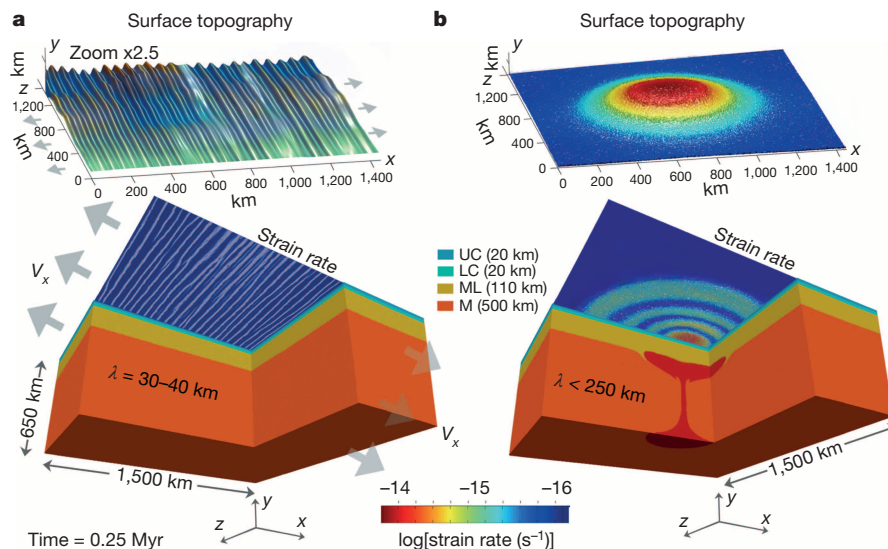


Figure 2 | Initial stages of end-member 3D numerical experiments. Top row, surface topography resulting from end-member cases of plume–lithosphere interactions (bottom row). Shown also in the bottom row are corresponding surface strain rate fields and the material phase field. **a**, No plume, and ultra-slow unidirectional tectonic extension (at a rate $V_x = 3 \text{ mm yr}^{-1}$) applied to a 250-Myr-old continental lithosphere. Note distributed closely spaced sub-parallel small-offset fault patterns spaced at $\lambda \approx 30\text{--}40 \text{ km}$. **b**, A 200-km plume initialized at 650-km depth impinges on the bottom of non-prestressed lithosphere. Note axisymmetric surface undulations with wavelengths (λ) of $<250 \text{ km}$ (150–250 km). Surface strain rate fields, or distributions, characterize the rates of surface deformation and topography evolution, ranging from fast ($>10^{-14} \text{ s}^{-1}$) to slow ($<10^{-16} \text{ s}^{-1}$). ML, mantle lithosphere; UC, upper crust; LC, lower crust; M, sub-lithosphere mantle. See also Extended Data Figs 1, 5, 7. The topography in **a** has a 2.5 vertical exaggeration compared to **b**.

determined by the far-field stress field and brittle localization in the lithosphere. The large-offset faults become increasingly important above the plume head, while almost no faulting occurs at distance larger than 200 km from the centre of rifting. Faults soon merge into a localized, linear rift, which opens at a significantly faster (5 to 10 times) rate than that of the ultra-slow passive extension applied at the borders (a 80-km-wide rift forms in less than 2.5 Myr while the amount of extension applied at the borders is only 7.5 km), showing that in this case the major driving force of rifting is active mantle upwelling. As predicted⁷, rifting creates a rift-parallel conduit for the flow of the plume material away from the region underlain by the starting plume head, further enhancing localized thinning of the lithosphere. The large-scale deformation becomes ‘cylindrical’, that is, two-dimensional, resembling a ‘typical’ continental rift (Extended Data Figs 5b, 6). The evolution of topography is summarized in Fig. 4: the initial surface response ($<1.5 \text{ Myr}$) is axisymmetric, as in the case of Fig. 2b, with large-scale subsidence evolving into a large-scale 1-km-high dome that narrows (300 km) and becomes more elevated with time ($>1.5 \text{ km}$). During the following few Myr, small-scale faulting is superimposed on a long-wavelength topography, which vanishes after 5–6 Myr. Further surface topography evolution is dominated by localized tectonic-scale rift structures. It is noteworthy that pre-rift doming is largely reduced.

In the next series of 3D experiments (Extended Data Fig. 7, 8), far-field velocities were applied at four sides of the model to produce a combination of simple and pure shear. The plume–lithosphere interaction then triggers formation of a sub-diagonal large-scale normal-and-strike-slip fault segmented by oblique Riedel shears. The fault has small lateral displacement ($<10\%$ of its length) and nucleates by the simultaneous coalescence of small-scale shears along the entire length of the rift. Interestingly, the surface topography resembles an early stage of a segmented spreading centre with a strong strike-slip component (for example, the Dead Sea rift and the Gulf of Aden). The same experiment implemented without mantle upwelling (Extended Data Fig. 7) shows only a series of distributed small-scale conjugated fault patterns.

We conclude from our modelling that localization of large-scale linear normal and strike-slip faults can be triggered and maintained by mantle flow that impacts the base of a pre-stressed lithosphere, so that the final state of the rifted lithosphere is an indicator of the far-field stress at the time the plume arrived. This suggests an efficient mechanism for continental rift initiation and breakup that involves passive and active rifting processes that interact with each other⁸, resulting in the development of large continental rifts (for example, the Afar, Gulf of Aden, Dead Sea, Baikal and East African rifts^{26,27}) and plate-scale strike-slip faults (for example, the Karakoum and North Anatolian faults¹⁰).

There is also a significant difference in the impact of the rheological profile on rifting style in the case of dominant active rifting compared to dominant passive rifting. Narrow rifting, conventionally attributed to cold strong lithosphere in passive rifting mode¹⁴, may develop in

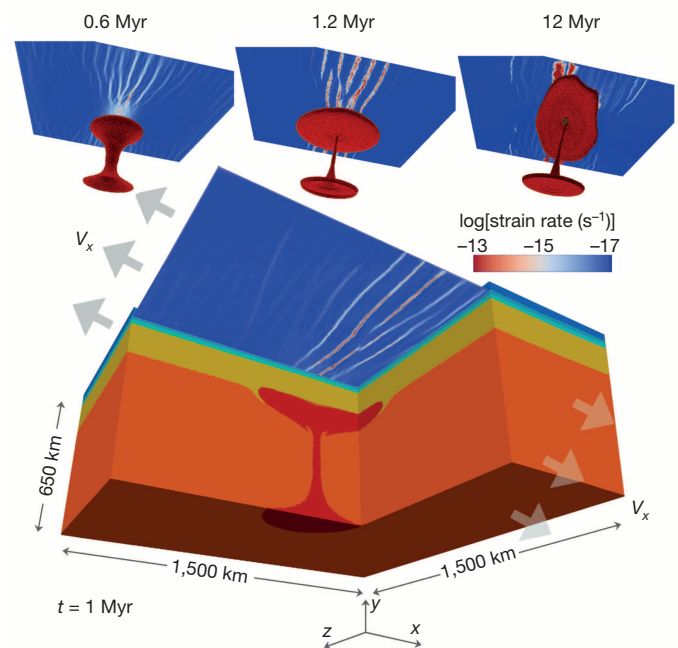


Figure 3 | Surface fault patterns and strain distributions in the case of plume–lithosphere interaction in the presence of a weak tectonic far-field stress field ($V_x = 3 \text{ mm yr}^{-1}$). The bottom panel shows the surface strain rate field (distribution) and the material phase field at time $t = 1 \text{ Myr}$. The top row shows the time evolution of the surface strain rate field (white to red colour, fast surface topography movements) at several key stages ($t = 0.6 \text{ Myr}$, 1.2 Myr , 12 Myr) of plume–lithosphere interaction. See also Fig. 4 and Extended Data Fig. 6. Note progressive focusing and amplification of surface deformation (linear faults) above the plume, resulting in rapid localization of non-axisymmetric, uni-directional deformation (rifting) at the surface. Rifting results in the alignment of the plume with the rift axis, causing rift-parallel flow of plume material away from the region underlain by the starting plume head, which further accelerates localized thinning of the lithosphere and the lithosphere break-up process. The lithosphere deformation soon becomes ‘cylindrical’, almost two-dimensional, resembling a ‘typical’ continental rift.

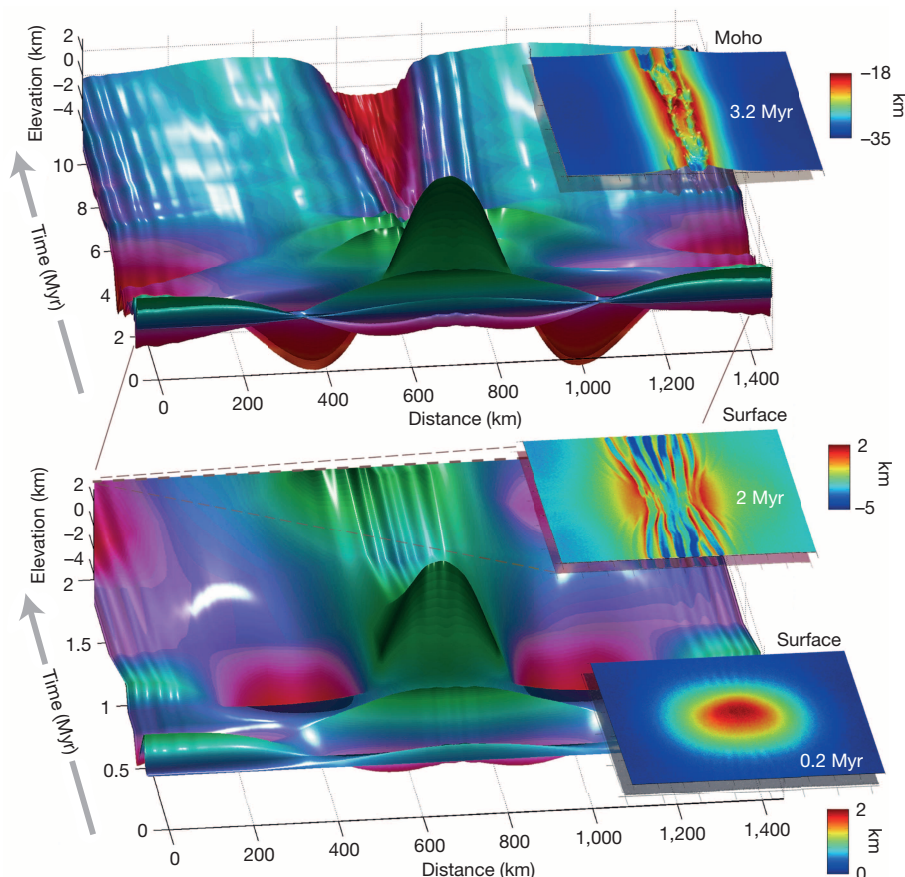


Figure 4 | Summary of time evolution of representative topography profile x, y . Top panel, overall time evolution of surface topography along a profile that runs through the centre of the model in the direction of extension (experiment shown in Fig. 3). Bottom panel, a zoom to the first, most important stages (1–2 Myr) of surface evolution. The rectangular insets show surface and Moho topography at key stages of time evolution (see Extended Data Fig. 6 for more details); colour bars with units of km correspond to vertical amplitudes of these topographies. Note initially short-lived axisymmetric domal uplift, which is rapidly followed by narrow, almost two-dimensional, rifting patterns. The lineation of these rifts is normal to the tectonic stress field direction. After 2 Myr, surface deformation patterns have shorter wavelengths than Moho topography.

weak hot ultra-stretched lithosphere during active rifting, after plume impingement on a tectonically pre-stressed lithosphere. In that case, initially ultra-wide small-amplitude rift patterns focus, in few Myr, into large-scale faults that form a narrow rift. Also, wide rifting may develop during ultra-slow spreading of strong lithosphere, and ‘switch’ to narrow rifting upon plume impingement.

Interplay between mantle–lithosphere interactions, rheological structure and intraplate stresses can result in two main topographic evolution scenarios: (1) in the general case of rheologically stratified lithosphere (with thermo-tectonic ages of 50–500 Myr; ref. 13), the topography exhibits short wavelengths ($\lambda \approx 50, 100, 350$ km) that are much smaller than those of mantle flow ($\lambda > 1,000$ km). In the presence of even a weak pre-existing far-field forcing, the topography is strongly asymmetric and is shaped by faults and rifts. (2) In the case of young and weak (age < 50 Myr) or old and strong plates (> 700 Myr ago, shields), the dynamic topography has ‘classical’ features, that is, it correlates with large-scale mantle flow.

Online Content Methods, along with any additional Extended Data display items and Source Data, are available in the online version of the paper; references unique to these sections appear only in the online paper.

Received 5 March; accepted 18 July 2014.

1. Lithgow-Bertelloni, C. & Silver, P. G. Dynamic topography, plate driving forces and the African superswell. *Nature* **395**, 269–272 (1998).
2. Moucha, R. & Forte, A. M. Changes in African topography driven by mantle convection. *Nature Geosci.* **4**, 707–712 (2011).
3. Hager, B. H., Clayton, R. W., Richards, M. A., Comer, R. P. & Dziewonski, A. M. Lower mantle heterogeneity, dynamic topography and the geoid. *Nature* **313**, 541–545 (1985).
4. Van der Hilst, R. D., Widiyantoro, S. & Engdahl, E. R. Evidence for deep mantle circulation from global tomography. *Nature* **386**, 578–584 (1997).
5. Guillou-Frotier, L., Burov, E., Nehlig, P. & Wyns, R. Deciphering plume-lithosphere interactions beneath Europe with topographic signatures. *Glob. Planet. Change* **58**(Spec. vol. on topography of Europe), 119–140 (2007).

6. Burov, E. & Guillou-Frotier, L. The plume head-lithosphere interaction using a tectonically realistic formulation for the lithosphere. *Geophys. J. Int.* **161**, 469–490 (2005).
7. Sleep, N. Lateral flow and ponding of starting plume material. *J. Geophys. Res.* **102**, 10001–10012 (1997).
8. Courtillot, V., Jaupart, C., Manighetti, I., Tapponnier, P. & Besse, J. On causal links between flood basalts and continental breakup. *Earth Planet. Sci. Lett.* **166**, 177–195 (1999).
9. Flament, N., Gurnis, M. & Müller, R. D. A review of observations and models of dynamic topography. *Lithosphere* **5**, 189–210 (2013).
10. Faccenna, C. & Becker, T. W. Shaping mobile belts by small-scale convection. *Nature* **465**, 602–605 (2010).
11. Anderson, D. L. The sublithospheric mantle as the source of continental flood basalt: the case against the continental lithosphere and plume head reservoirs. *Earth Planet. Sci. Lett.* **123**, 269–280 (1994).
12. Molnar, P. & Houseman, G. A. The effects of buoyant crust on the gravitational instability of thickened mantle lithosphere at zones of intracontinental convergence. *Geophys. J. Int.* **158**, 1134–1150 (2004).
13. Burov, E. B. Rheology and strength of the lithosphere. *Mar. Petrol. Geol.* **28**, 1402–1443 (2011).
14. Buck, R. in *Treatise on Geophysics* Vol. 6, *Crust and Lithosphere Dynamics* (ed. Watts, T.) 335–376 (Elsevier, 2007).
15. Burov, E., Guillou-Frotier, L., d’Acremont, E., Le Pourhiet, L. & Cloetingh, S. Plume head–lithosphere interactions near intra-continental plate boundaries. *Tectonophysics* **434**, 15–38 (2007).
16. Sleep, N. H., Ebinger, C. J. & Kendall, J.-M. in *The Early Earth: Physical, Chemical and Biological Development* (eds Fowler, C. M. R., Ebinger, C. J. & Hawkesworth, C. J.) 135–150 (Geological Society of London Spec. Publ. 199, 2002).
17. Lin, S. C. & van Keken, P. E. Multiple volcanic episodes of flood basalts caused by thermochemical mantle plumes. *Nature* **436**, 250–252 (2005).
18. Boher, M., Abouchami, W., Michard, A., Albarède, F. & Arndt, N. T. Crustal growth in west Africa at 2.1 Ga. *J. Geophys. Res.* **97**, 345–369 (1992).
19. Lustrino, M. & Carminati, E. Phantom plumes in Europe and the circum-Mediterranean region. *Geol. Soc. Am. Spec. Publ.* **430**, 723–745 (2007).
20. Molnar, P. & Houseman, G. A. Rayleigh–Taylor instability, lithospheric dynamics, surface topography at convergent mountain belts, and gravity anomalies. *J. Geophys. Res.* **118**, 2544–2557 (2013).
21. Foulger, G. R. *et al.* The seismic anomaly beneath Iceland extends down to the mantle transition zone and no deeper. *Geophys. J. Int.* **142**, F1–F5 (2000).
22. Sun, D., Helmberger, D. & Gurnis, M. A narrow mid-mantle plume below southern Africa. *Geophys. Res. Lett.* **37**, L09302 (2010).

23. Collins, J. A., Wolfe, C. J. & Laske, G. Shear wave splitting at the Hawaiian hot spot from the PLUME land and ocean bottom seismometer deployments. *Geochem. Geophys. Geosyst.* **13**, Q02007 (2012).
24. Davies, G. F. Temporal variation of the Hawaiian plume flux. *Earth Planet. Sci. Lett.* **113**, 277–286 (1992).
25. Wessel, P. & Keating, B. H. Temporal variations of flexural deformation in Hawaii. *J. Geophys. Res.* **99**, 2747–2756 (1994).
26. Pik, R., Marty, R. & Hilton, D. R. How many mantle plumes in Africa? The geochemical point of view. *Chem. Geol.* **226**, 100–114 (2006).
27. Moreira, M., Valbracht, P. J., Staudacher, T. & Allègre, C. J. Rare gas systematics in Red Sea ridge basalts. *Geophys. Res. Lett.* **23**, 2453–2456 (1996).
28. Ueda, K., Gerya, T. & Sobolev, S. V. Subduction initiation by thermal–chemical plumes: numerical studies. *Phys. Earth Planet. Inter.* **171**, 296–312 (2008).
29. Burov, E. & Cloetingh, S. Controls of mantle plumes and lithospheric folding on modes of intra-plate continental tectonics: differences and similarities. *Geophys. J. Int.* **37**, L03309 (2010).
30. Gerya, T. V. *Introduction to Numerical Geodynamic Modelling* (Cambridge Univ. Press, 2010).

Acknowledgements B. Evans and P. Molnar are thanked for discussions. A. B. Watts is thanked for comments on the manuscript and corrections to it. This study was co-funded by an Advanced ERC grant RHEOLITH (E.B.), by INSU-CNRS, by a UPMC Invited Professor grant (T.G.) and by an ETH Invited Professor grant (E.B.). Numerical simulations were performed on the ETH Brutus cluster and on the ERC-funded SGI Ulysse cluster of ISTEP (UPMC). Open source software ParaView (<http://www.paraview.org>) was used for 3D visualization.

Author Contributions E.B. designed the study, conducted some of the 3D experiments, designed the 2D thermo-mechanical code and conducted 2D experiments. T.G. designed the 3D thermo-mechanical code and conducted some of the 3D experiments. Both authors discussed problems and methods, interpreted the data and wrote the paper.

Author Information Reprints and permissions information is available at www.nature.com/reprints. The authors declare no competing financial interests. Readers are welcome to comment on the online version of the paper. Correspondence and requests for materials should be addressed to E.B. (evgenii.burov@upmc.fr).

METHODS

General features of the numerical models. The numerical 3D code I3ELVIS is based on a combination of a finite difference method, applied on a staggered Eulerian grid, and a marker-in-cell technique^{30,31}. The momentum, continuity and energy equations are solved on the Eulerian frame, and physical properties are transported by Lagrangian markers that move according to the velocity field interpolated from the fixed grid. Non-newtonian viscous-plastic rheologies are used in the model (Extended Data Tables 1, 2), which is also fully thermodynamically coupled and accounts for mineralogical phase changes, adiabatic, radiogenic and frictional internal heating sources. The free surface topography is reproduced using the 'sticky air' technique³⁰ enhanced by the introduction of a high-density marker distribution in the near-surface zone (Extended Data Fig. 1). Full details of this method, allowing for its reproduction, are provided elsewhere³⁰. The complementary 2D experiments (Extended Data Figs 1–4) implementing true high-precision free surface and non-newtonian viscous-elastic-plastic rheology employ the Flamar code²⁹, which uses the robust FLAC²⁹ algorithm based on a fully Lagrangian formulation allowing for precision tracking of surface topography. The 2D experiments were used for preliminary parametric tests aimed at reducing the tested parameter range in 3D, and for verification of topography amplitudes and radial topography spectra predicted by 3D models. This well-tested algorithm has been used for plume and mantle–lithosphere interaction problems in many previous studies^{6,15,29}.

Numerical model design. In the 3D experiments implemented with I3ELVIS, the regular rectangular Eulerian grid has a spatial resolution of $3 \times 3 \times 3$ km and comprises $500 \times 500 \times 217$ nodes filled with half a billion randomly distributed Lagrangian markers. The spatial dimensions of the model are, accordingly, $1,500 \times 1,500 \times 650$ km. Some experiments were implemented with spatial grid resolutions of $2 \times 2 \times 2$ km (spatial dimensions $1,000 \times 1,000 \times 650$ km) and $5 \times 5 \times 5$ km (spatial dimensions $2,000 \times 2,000 \times 650$ km). The 3D model setup is described in the main text and depicted in Fig. 2 and Extended Data Fig. 1.

To reduce 3D computational efforts by narrowing the explored parameter range, as well as to conduct additional cross-checking of the results with an accurate independent code, we first implemented a series of 'fast' 2D parametric tests (Extended Data Fig. 1), combining them with the inferences from previous rheologically realistic 2D models^{6,15,29}. This has allowed us to limit the tested thermo-tectonic age range to 75–450 Myr ago, and the range of the tested diameters of mantle upwellings to 150–300 km (the tests have shown that smaller plumes have limited impact while bigger ones produce a predictably larger effect⁶). Following the results of the 2D parametric experiments, the reference plume size has been fixed at 200 km and the thermo-tectonic age of 150-km-thick lithosphere at 250 Myr ago²⁹. During these tests we actually used both the main code I3ELVIS executed in '2D' mode and the Lagrangian 2D code Flamar²⁹ that implements an explicit free surface, which makes it potentially more accurate in reproduction of surface topography (Extended Data Fig. 1b).

The 3D and 2D models²⁹ have, as much as possible, an identical design (Extended Data Fig. 1). It comprises a stratified three-layer continental lithosphere composed of upper crust, lower crust and lithospheric mantle placed on top of the upper mantle. The starting geometry of the mantle plume corresponds to a sphere with a diameter of 200 km initially located at the bottom of the model. The total crustal thickness is 40 km. The rheology of the upper and lower crust corresponds to that of wet granite and diabase, respectively (Extended Data Table 2). The thickness of each crustal layer is 20 km. The depth to the bottom of the lithosphere is 150 km. The rheological properties of the mantle lithosphere and of the sub-lithosphere mantle correspond to those of dry olivine (Extended Data Table 2). The initial lithospheric geotherm is calculated as function of the assumed thermo-tectonic age^{6,13}. The initial mantle geotherm is adiabatic below the lithosphere. The boundary conditions at the upper surface and at the bottom of the model are 0°C and $1,600$ – $1,700^\circ\text{C}$, respectively. The initial temperature at the bottom of the lithosphere is $1,330^\circ\text{C}$, yielding an initial adiabatic temperature gradient in the mantle of the order of 0.5 – $0.7^\circ\text{C km}^{-1}$. The plume has an initial temperature of $2,000^\circ\text{C}$. Zero horizontal heat flux is assumed across the lateral (vertical) boundaries. As mechanical boundary conditions, we apply divergence velocities at the appropriate sides of the model. In 3D models, compensating vertical influx velocities through the upper and lower boundaries are introduced to ensure mass conservation in the model domain; free slip boundary conditions are used on the sides that are not subject to extension or compression.

The initial configuration of the model corresponds to a general scenario^{6,29}, in which the model experiment begins at the moment when the deep mantle plume has just arrived at the interface between the upper and lower mantle at 650 km depth and started its ascent to the surface through the upper mantle. It is generally accepted (except for 'baby plumes') that plumes ascend from great depth³² in two stages: a slow, long primary stage in the high-viscosity lower mantle (small, near-critical, Rayleigh number), and a rapid stage in the low-viscosity upper mantle (high Rayleigh number^{6,29}, 10^5 – 10^7). When the lower-mantle plume ascends through the phase change barrier between the upper and lower mantle at 650 km depth, it undergoes

radical transformations³², so that it can be considered as a 'new' plume instantly generated at 650 km depth. As mentioned in the main text, under this scenario, the initial surface uplift and subsidence events ($t < 0.5$ – 1 Myr, Fig. 4, Extended Data Fig. 5) are caused by interplay between the dynamic push, temperature and buoyancy of the plume, the isostatic effect of mechanical erosion and thinning of the LAB due to the mantle flow above the upwelling plume head, and gravitational Rayleigh–Taylor instability that develops in chemically un-depleted dense mantle lithosphere destabilized by LAB erosion and lower-density plume upwelling. During the first 0.1 – 1 Myr, the lowermost part of the light, weak, hot mantle lithosphere is mechanically eroded by mantle flow above the upwelling plume, leaving a stronger, cold, dense, gravitationally unstable lithospheric mantle 'core'. As result, the dense mantle lithosphere develops a Rayleigh–Taylor instability and sags down towards the lower density plume head, in accordance with the predictions of previous rheologically realistic 2D studies⁶. This effect is facilitated by rheological stratification of the continental lithosphere. It is noteworthy that the eventual detachment of the down-warped dense mantle–lithosphere 'blob' causes localized isostatic uplift at the surface. Hence, the initial large-scale subsidence is superimposed on narrower central doming caused by LAB instabilities and the dynamic impact and buoyancy of the mantle plume (see Fig. 4 at ~ 0.5 – 1.5 Myr). Starting from $t = 0.5$ Myr, the buoyancy and dynamic push from the arriving plume increases, producing large-scale uplift. Uplifts and subsidence events due to plume/lithosphere interplay continue for several Myr until lithospheric rifting starts to dominate surface topography.

Viscous-plastic rheological model. The viscous and brittle (plastic) properties (see Extended Data Tables 1, 2) are implemented via evaluation of the effective viscosity of the material. For the ductile materials, the contributions from different flow laws such as dislocation, diffusion and Peierls creep (due to computational speed issues included in the 2D models only) are taken into account via computation of inverse average viscosity. For example, for a material experiencing diffusion and dislocation creep, characterized by effective viscosities η_{newt} and η_{powl} , respectively, the average viscosity η (or η_{ductile}) is defined by:

$$\frac{1}{\eta_{\text{ductile}}} = \frac{1}{\eta_{\text{newt}}} + \frac{1}{\eta_{\text{powl}}} \quad (1)$$

where η_{newt} and η_{powl} are calculated from equations for newtonian diffusion creep and power law dislocation creep, respectively:

$$\eta_{\text{newt}} = \frac{1}{2} \frac{A_D}{\sigma_{\text{cr}}^{n-1}} e^{\frac{E+PV}{RT}} \quad (2)$$

$$\eta_{\text{powl}} = \frac{1}{2} \left(A_D e^{\frac{E+PV}{RT}} \right)^{\frac{1}{n}} \frac{1}{\dot{\epsilon}_{II}^{\frac{1-n}{n}}} \quad (3)$$

where P is the dynamic pressure, T is temperature (in K), $\dot{\epsilon}_{II} = \sqrt{\frac{1}{2} \dot{\epsilon}_{ij} \dot{\epsilon}_{ij}}$ is the second invariant of the strain rate tensor and A_D , E , V , n and σ_{cr}^{n-1} are experimentally determined flow law parameters (Extended Data Table 2), which stand for the material constant, the activation energy, the activation volume, the stress exponent and the diffusion-dislocation transition stress, respectively. The ductile rheology is combined with a brittle/plastic rheology to yield an effective viscous-plastic rheology characterized by the effective viscosity η_{plastic} :

$$\eta_{\text{plastic}} = \frac{\sigma_{\text{yield}}}{2\dot{\epsilon}_{II}} \quad (4)$$

where σ_{yield} is the yield stress.

The Drucker–Prager yield criterion for brittle behaviour is implemented as follows:

$$\sigma_{\text{yield}} = C + P \sin(\varphi) \quad (5)$$

Here P is pressure and the residual rock strength C and the internal frictional angle φ are defined by

$$C = \tilde{N}_0 + (\tilde{N}_1 - \tilde{N}_0) \frac{\varepsilon - \varepsilon_0}{\varepsilon_1 - \varepsilon_0} \quad (6)$$

$$\varphi = \arcsin \left(b_0 + (b_1 - b_0) \frac{\varepsilon - \varepsilon_0}{\varepsilon_1 - \varepsilon_0} \right) \quad (7)$$

where ε is the second invariant of strain and \tilde{N}_0 , \tilde{N}_1 , b_0 , b_1 , ε_0 and ε_1 are softening parameters provided in Extended Data Table 1. Brittle rheology results in localized anisotropic deformation, for example, in formation of conjugate faults making an angle $\sim \frac{1}{2}(\pi - \varphi)$ with principal stress direction.

With η_{ductile} and η_{plastic} , the visco-plastic rheology is assigned to the model by means of a Christmas-tree-like criterion, where the rheological behaviour depends on the minimum viscosity (or differential stress) attained between the ductile and brittle/plastic fields:

$$\eta = \min(\eta_{\text{ductile}}, \eta_{\text{plastic}}) \quad (8)$$

Governing equations. The numerical code I3DELVIS solves momentum, continuity and heat conservation equations for 3D creeping flow. Its numerical schema is based on finite differences with a marker-in-cell technique, which allows for non-diffusive numerical simulation of multiphase flow in a rectangular fully staggered Eulerian grid^{30,31}. Owing to the Eulerian framework, free surface is implemented using the ‘sticky air’ approximation, with a 30-km-thick effectively weightless ‘air’ layer²⁸ with viscosity of 10^{18} Pa s on top of the model lithosphere. These ‘sticky air’ parameters provide an optimal compromise between the accuracy of the free-surface reproduction and the numerical performance (see below; Extended Data Fig. 1b, see also discussion at the end of Methods). A fully detailed version of the code description provided below can be found elsewhere³⁰.

The momentum equations are presented in the form of the Stokes flow approximation:

$$\begin{aligned} \frac{\partial \tau_{xx}}{\partial x} + \frac{\partial \tau_{xy}}{\partial y} + \frac{\partial \tau_{xz}}{\partial z} &= \frac{\partial P}{\partial x}, \\ \frac{\partial \tau_{yx}}{\partial x} + \frac{\partial \tau_{yy}}{\partial y} + \frac{\partial \tau_{yz}}{\partial z} &= \frac{\partial P}{\partial y} - \rho g, \\ \frac{\partial \tau_{zx}}{\partial x} + \frac{\partial \tau_{zy}}{\partial y} + \frac{\partial \tau_{zz}}{\partial z} &= \frac{\partial P}{\partial z}, \end{aligned} \quad (9)$$

where τ_{ij} are the components of the viscous deviatoric stress tensor, ρ is the density dependent on rock composition, temperature and pressure, and g is the acceleration due to gravity.

Conservation of mass is approximated by the continuity-compatibility equation:

$$\frac{\partial v_x}{\partial x} + \frac{\partial v_y}{\partial y} + \frac{\partial v_z}{\partial z} = \nabla \cdot \mathbf{v} = 0 \quad (10)$$

where v_x , v_y and v_z are components of the velocity vector.

The components of the deviatoric stress tensor are calculated using the viscous constitutive relationship between stress and strain rate:

$$\tau_{ij} = \eta(\dot{\epsilon}_{ij} + \dot{\epsilon}_{ji}) \quad (11)$$

where the components of shear strain rate tensor are:

$$\dot{\epsilon}_{ij} = \frac{1}{2} \left(\frac{\partial v_i}{\partial x_j} + \frac{\partial v_j}{\partial x_i} \right) \quad (12)$$

The mechanical equations are coupled with heat conservation equations:

$$\begin{aligned} \rho C_p \left(\frac{\partial T}{\partial t} \right) &= - \frac{\partial q_x}{\partial x} - \frac{\partial q_y}{\partial y} - \frac{\partial q_z}{\partial z} + H_r + H_a + H_s, \\ q_x &= -k \frac{\partial T}{\partial x}, q_y = -k \frac{\partial T}{\partial y}, q_z = -k \frac{\partial T}{\partial z}, \end{aligned} \quad (13)$$

where C_p is the heat capacity, k is the thermal conductivity, H_r is the radiogenic heat production and H_a and H_s are the contributions due to isothermal (de)compression (that is, adiabatic heating/cooling) and the shear heating, respectively:

$$H_a = \frac{\alpha T \rho v_y g}{1 - \alpha(T - T_0)} \quad (14)$$

$$H_s = \tau_{xx} \dot{\epsilon}_{xx} + \tau_{yy} \dot{\epsilon}_{yy} + \tau_{zz} \dot{\epsilon}_{zz} + 2\tau_{xy} \dot{\epsilon}_{xy} + 2\tau_{yz} \dot{\epsilon}_{yz} + 2\tau_{xz} \dot{\epsilon}_{xz} \quad (15)$$

where $T_0 = 298$ K and α is the coefficient of thermal expansion.

Petrological phase changes are implemented using a thermodynamic solution for density, $\rho = f(P, T)$, obtained from optimization of Gibbs’ free energy for a typical mineralogical composition of the mantle, plume and lithosphere material. With that goal, the thermodynamic PERPLEX algorithm and the associated petrological database³³ has been coupled with the main code to introduce progressive changes in density and other material properties. PERPLEX minimizes free Gibbs’ energy G for a given chemical composition to calculate an equilibrium mineralogical assemblage for given P – T conditions:

$$G = \sum_{i=1}^n \mu_i N_i \quad (16)$$

where μ_i is the chemical potential and N_i the mole number for each component i constitutive of the assemblage. Given the mineralogical composition, the computation of density is straightforward.

2D modelling experiments. For ultra-high-resolution (element sizes 1×1 km and 2×2 km for the entire computation domain) 2D experiments used for parametric study (Extended Data Figs 1–4), we cross-checked a 2D implementation of I3DELVIS with the free-surface 2D code Flamar v12³⁴ based on the FLAC algorithm³⁵. As mentioned in the main text, Flamar has been chosen because of its previous successful application to the problems of plume–lithosphere interactions^{6,15,29} and tectonic deformation³⁴ warranted by its explicit Lagrangean free-surface implementation that provides high accuracy for surface topography. During these experiments, we have tested Flamar using Cramer’s benchmark test³⁶ for plume upwelling, where it has demonstrated an order of 1 m accuracy for an element size of 3×3 km. Unlike Flamar, I3DELVIS (and other Eulerian codes used in geotectonics³⁶) implements the ‘sticky air’ approximation to reproduce free-surface topography^{36,37}. The benchmark tests of the 2D version of I3DELVIS (I2VIS) for plume upwelling have shown a largely sufficient accuracy (<50 m for 3.3 km grid spacing) in reproduction of the free surface³⁶ for a ‘sticky layer’ of thickness ≥ 30 km and viscosity $\leq 10^{19}$ Pa s (see also Extended Data Fig. 1b). This accuracy, however, has been obtained for the simple case of linear viscous rheology³⁶, so additional cross-checking of the results with an independent free-surface code was used to ensure the robustness of the results. The results of 2D experiments implemented with two different codes (Flamar and 2D implementation of I3DELVIS) have demonstrated very good compatibility (Extended Data Fig. 1a). These tests were particularly encouraging, since, while solving the same thermo-mechanical problems as I3DELVIS, Flamar uses a very different, independent numerical scheme.

Unlike I3DELVIS, Flamar employs a fully explicit hybrid finite element/finite difference time-marching Lagrangian scheme solving Newtonian equations of motion in full stress formulation (that encompass equation (9) under equivalent conditions):

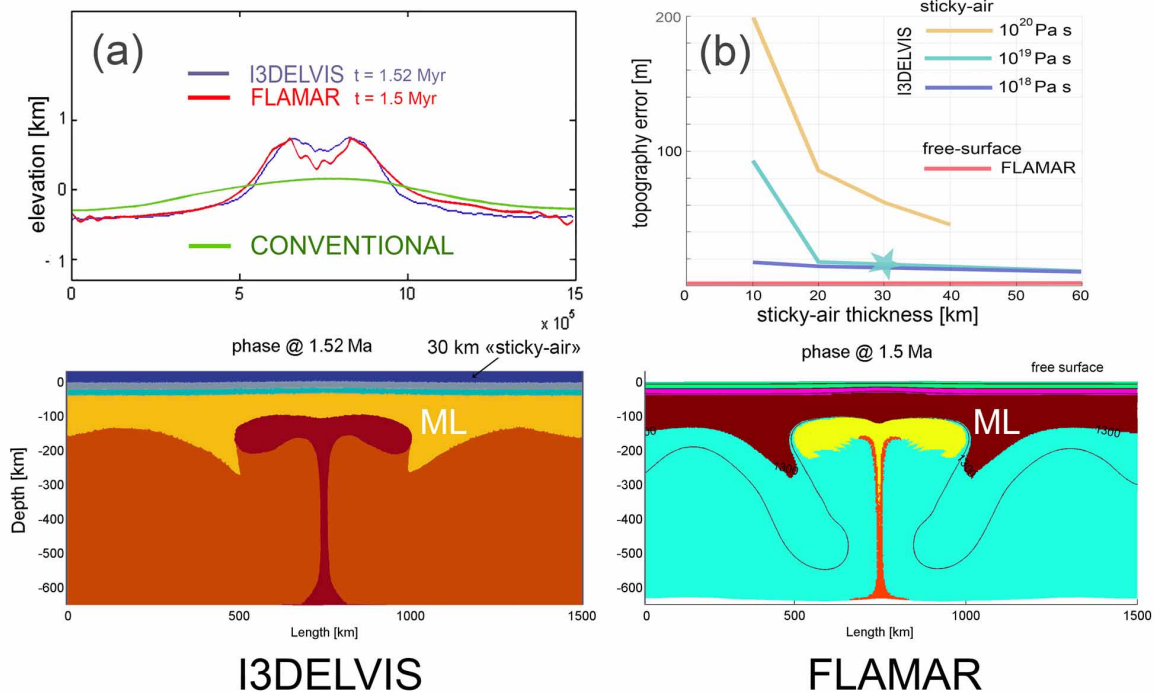
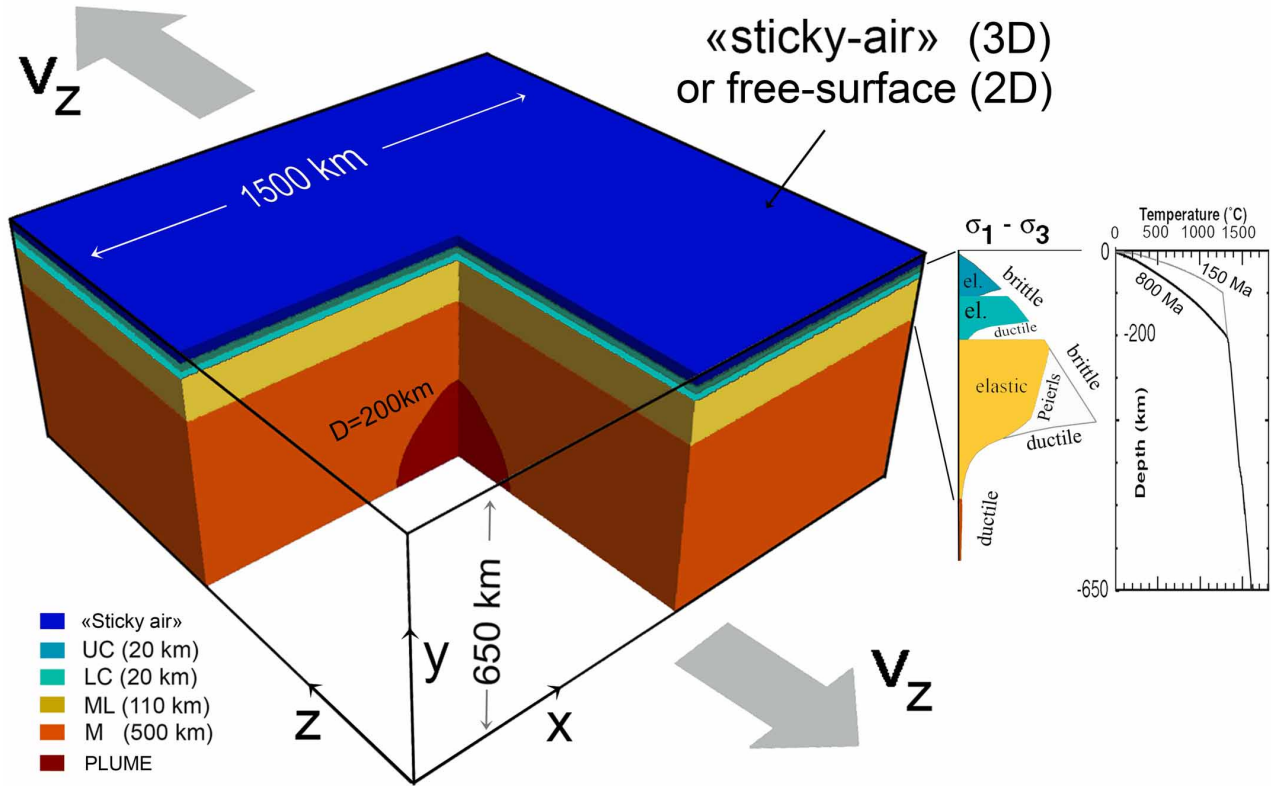
$$\rho_{\text{inert}} \frac{dv_i}{dt} = \frac{\partial \sigma_{ij}}{\partial x_j} + \rho g_i \quad (17)$$

where σ is full stress, that is, $\frac{\partial \sigma_{ij}}{\partial x_j} = \frac{\partial \tau_{ij}}{\partial x_j} + \frac{\partial p}{\partial x_i}$, g_i is component i of acceleration

due to gravity, ρ_{inert} corresponds to the inertial density, that is, $\rho_{\text{inert}} = \rho$ in the dynamic mode or $\rho_{\text{inert}} = \frac{\eta \text{Re}}{\nu L} \leq 0.01 \frac{\eta}{\nu L}$ in quasi-static mode, where L is the characteristic flow length and Re is the ‘numerical’ Reynolds number that must be smaller than 0.01 in the quasi-static regime³⁵. In FLAC/Flamar, all rheological terms are implemented explicitly, without using the equivalent viscosity for non-viscous terms. The other processes and properties implemented in the version of Flamar that has been adjusted for these experiments were set equivalent to those given by equations (1)–(3), (5)–(7) and (12)–(16). Flamar is specially adapted for solving nonlinear large-strain problems, while its numerical scheme is widely used and well-tested for nonlinear large-strain problems, thanks to its commercial engineering version (FLAC³⁵). It is noteworthy that accurate reproduction of surface deformation is warranted in Flamar not only by its explicit Lagrangean free surface implementation but also by its explicit time-marching scheme which allows for very short time steps (1–10 yr in our problem); hence it is devoid of surface stabilization issues that might eventually affect surface predictions in the implicit codes³⁷. Flamar also takes into account the elastic rheology ($\sigma_{ij} = \lambda_e \epsilon_{ii} \delta_{ij} + 2G_e \epsilon_{ij}$; see Extended Data Table 1, that is, this code is elastic-viscous-plastic), while, due computational speed issues, I3DELVIS disregards elasticity for long-term processes. We hence also used Flamar-based experiments to verify that elasticity has no particular importance in the framework of our study (Extended Data Fig. 1a). Successful comparison of the results of two independent codes made us particularly certain of the robustness of the experiments of this study.

- Gerya, T. V. & Yuen, D. A. Robust characteristics method for modelling multiphase visco-elasto-plastic thermo-mechanical problems. *Phys. Earth Planet. Inter.* **163**, 83–105 (2007).
- Goes, S., Spakman, W. & Bijwaard, H. A lower mantle source for central European volcanism. *Science* **286**, 1928–1931 (1999).
- Connolly, J. A. D. Computation of phase equilibria by linear programming: a tool for geodynamic modeling and its application to subduction zone decarbonation. *Earth Planet. Sci. Lett.* **236**, 524–541 (2005).
- Burov, E. & Yamato, Ph. Continental plate collision, P–T–t conditions and unstable vs. stable plate dynamics: Insights from thermo-mechanical modelling. *Lithos* **103**, 178–204 (2008).

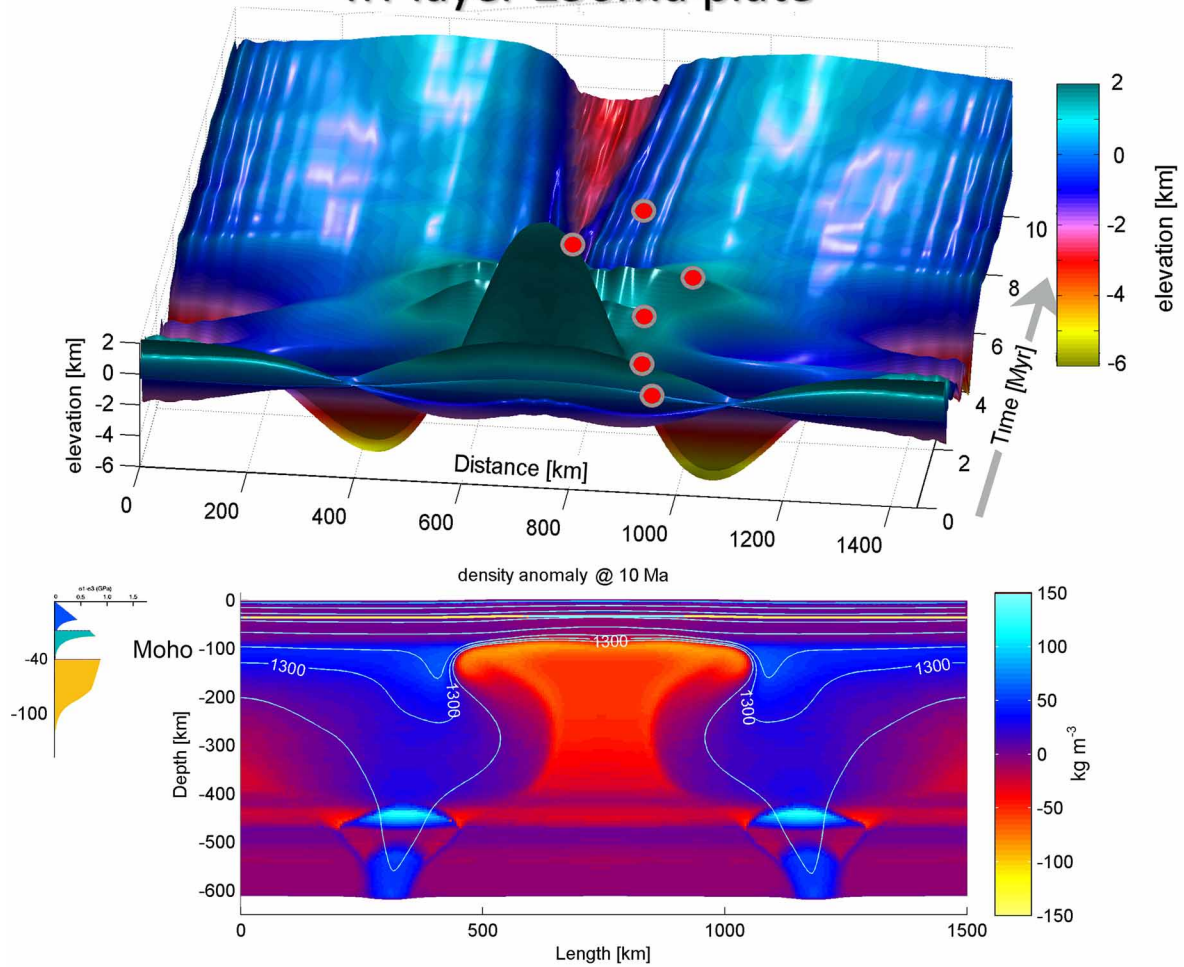
35. Cundall, P. A. Numerical experiments on localization in frictional materials. *Ingen. Arch.* **59**, 148–159 (1989).
36. Cramer, F. *et al.* A comparison of numerical surface topography calculations in geodynamic modelling: an evaluation of the 'sticky air' method. *Geophys. J. Int.* **189**, 38–54 (2012).
37. Duretz, T., May, D. A., Gerya, T. V. & Tackley, P. J. Discretization errors and free surface stabilization in the finite difference and marker-in-cell method for applied geodynamics: a numerical study. *Geochem. Geophys. Geosyst.* **12**, <http://dx.doi.org/10.1029/2011GC003567> (2011).
38. Turcotte, D. L. & Schubert, G. *Geodynamics* 2nd edn (Cambridge Univ. Press, 2002).
39. Goetze, C. & Evans, B. Stress and temperature in bending lithosphere as constrained by experimental rock mechanics. *Geophys. J. R. Astron. Soc.* **59**, 463–478 (1979).
40. Bürgmann, R. & Dresen, G. Rheology of the lower crust and upper mantle: evidence from rock mechanics, geodesy, and field observations. *Annu. Rev. Earth Planet. Sci.* **36**, 531–567 (2008).
41. Burov, E. Rheology and strength of the lithosphere. *Mar. Petrol. Geol.* **28**, 1402–1443 (2011).
42. Durham, W. B., Mei, S., Kohlstedt, D. L., Wang, L. & Dixon, N. A. New measurements of activation volume in olivine under anhydrous conditions. *Phys. Earth Planet. Inter.* **172**, 1–2: 67–73 (2009).
43. Karato, S.-I. & Wu, P. Rheology of the upper mantle: A synthesis. *Science* **260**, 771–778 (1993).
44. Carter, N. L. & Hansen, F. D. Creep of rocksalt. *Tectonophysics* **92**, 275–333 (1983).
45. Caristan, Y. The transition from high temperature creep to fracture in Maryland diabase. *J. Geophys. Res.* **87**, 6781–6790 (1982).
46. Ranalli, G. *Rheology of the Earth* 2nd edn (Chapman and Hall, 1995).



Extended Data Figure 1 | Numerical model set-up and tests of 3D and 2D models. Top panel shows the numerical model set-up. The initial plume-mantle temperature contrast ΔT is 300 °C. Lateral velocities (for example, V_x , V_y , V_z) are applied at two or four opposite sides of the model. Bottom panels, comparison of 2D implementation of I3DELVIS (left) with FLAMAR (right), for the experiment of Fig. 4 at $t \approx 1.5$ Myr. Middle panel **a** presents topographies (red and blue curves) generated by the models shown in the

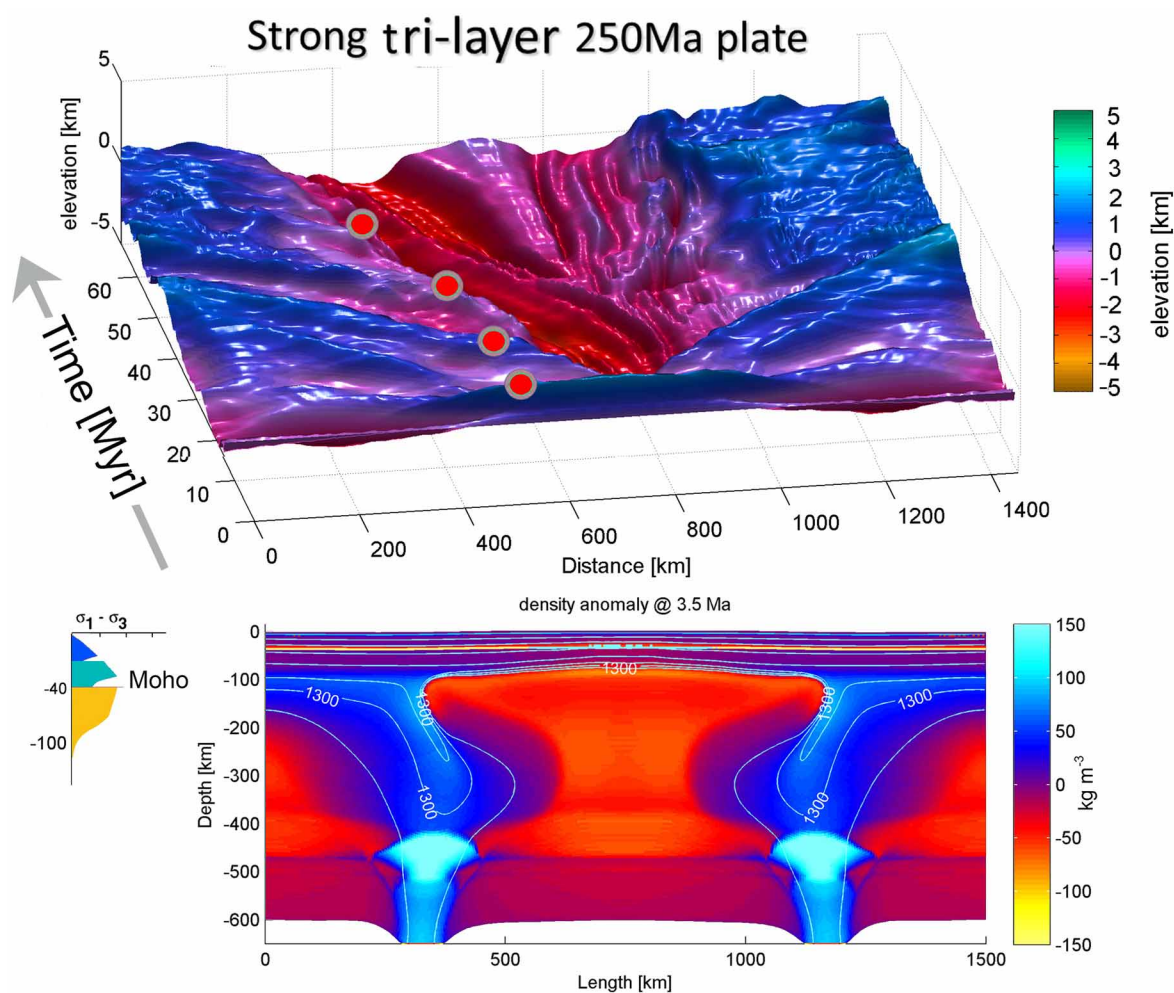
bottom panel. Green curve in **a** shows conventional dynamic topography (that is, filtered non-isostatic topography)². Middle panel **b** shows Crameri's topography precision benchmark test³⁶ (100-km-diameter plume rising below an isoviscous lithosphere³⁶). Star in **b** corresponds to 'sticky air' thickness and viscosity retained for computations (30 km, 10^{18} Pa s); colour curves in **b** correspond to tested sticky-air viscosities. See Methods for further details.

Tri-layer 250Ma plate



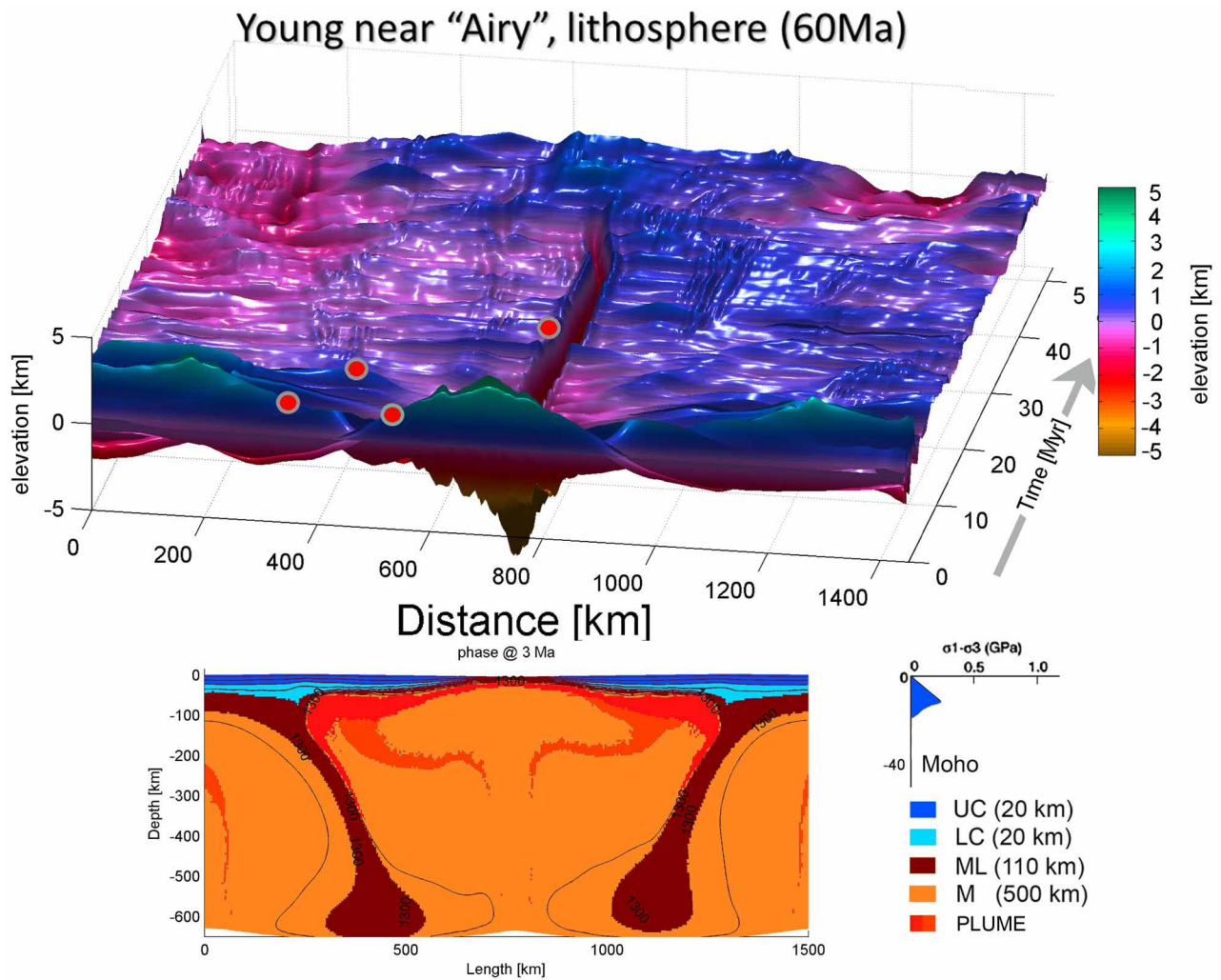
Extended Data Figure 2 | 2D experiment showing time evolution of surface topography for the reference case (lithosphere with a thermo-tectonic age of 250 Myr). Top, set-up of this 2D experiment is identical to that of the 3D experiments shown in Fig. 3. Far-field extension ($V_x = 3 \text{ mm yr}^{-1}$) is applied at both sides of the lithosphere. The red-grey circles mark major stages of

topography evolution (initial subsidence followed by large-scale doming, then by a more localized higher amplitude doming that progressively gets overprinted by rifting patterns). Note persistent short-wavelength features. Bottom, snapshot of density anomaly field at 10 Myr since the onset of plume initiation. Inset at left shows reference yield-stress envelope of the lithosphere.



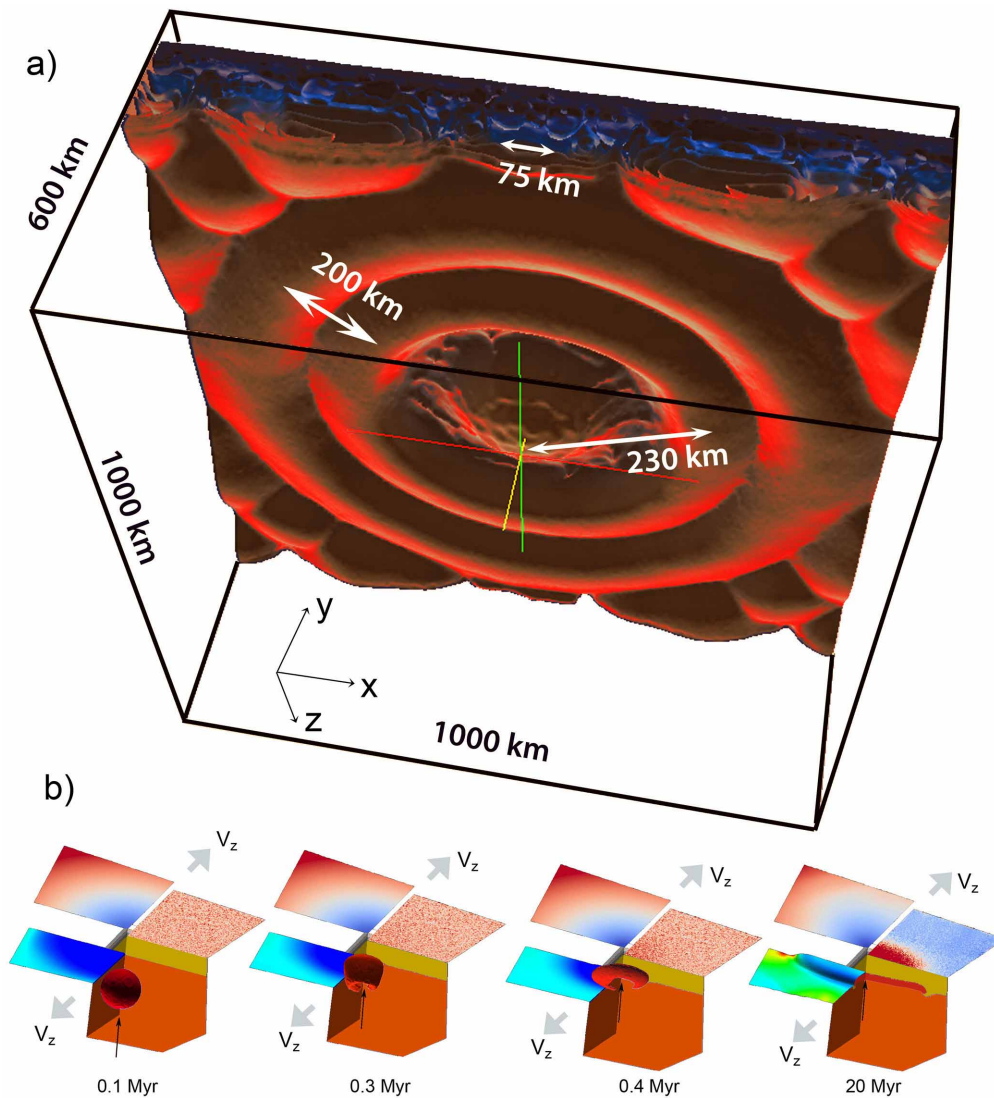
Extended Data Figure 3 | 2D experiment equivalent to that shown in Extended Data Fig. 2 but under the assumption of strong, dry, diabase lower crustal rheology. See Extended Data Fig. 2 legend for notation. Top, note

the difference in the surface and sub-surface dynamics (double-width rifting) from the case of Extended Data Fig. 2 with weaker lower crustal rheology. Bottom, note also phase density changes at the 410-km phase boundary.



Extended Data Figure 4 | 2D experiment equivalent to that shown in Extended Data Fig. 2 but under the assumption of hot, young, lithosphere with a thermo-tectonic age of 60 Myr. Top, note crucial differences in the dynamic topography compared to the cases of colder and stronger lithosphere.

Bottom, material field evolution (large-scale delamination of mantle lithosphere). Note delamination of the major part of the continental lithosphere mantle, which is being replaced by new lithosphere mantle formed from mantle plume material.

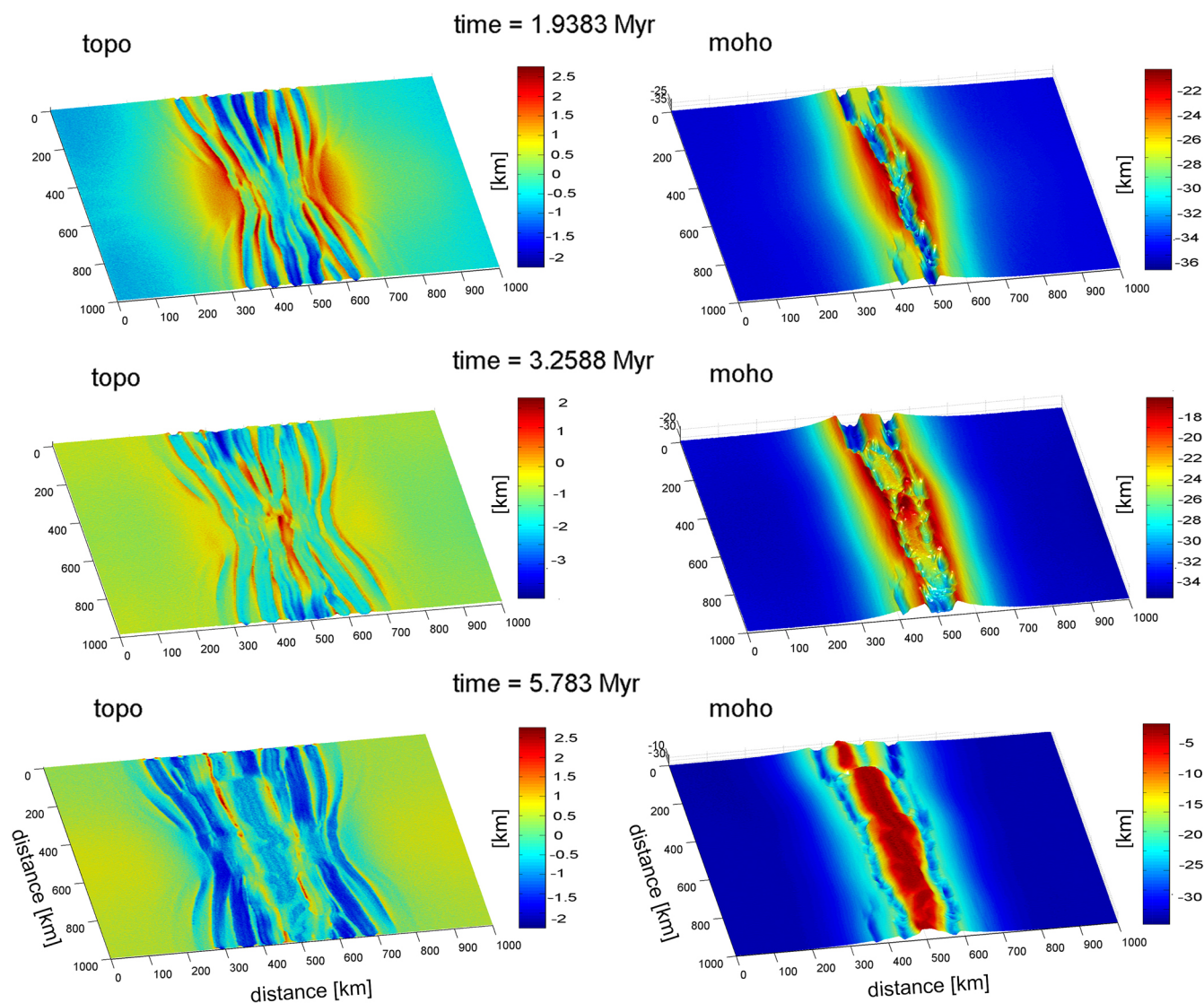


Extended Data Figure 5 | 3D deformation patterns at the bottom of the lithosphere in the case of plume impingement. **a**, 3D deformation patterns at lithosphere bottom in the absence of tectonic forcing (experiment similar to that of Fig. 2b at 0.5 Myr). Note periodic axisymmetric undulations with short wavelengths λ (30–250 km), in agreement with 2D models (Extended Data Fig. 2, Methods). Central down-warping is caused by Rayleigh–Taylor

instability in dense mantle lithosphere, which is destabilized by plume ascent. **b**, Time evolution of plume–lithosphere interaction in the case of unidirectional far-field stretching ($V_x = 3 \text{ mm yr}^{-1}$, experiment of Fig. 3). Note progressive channelized alignment of plume head material along the rift axis accelerating localization of the rift zone.

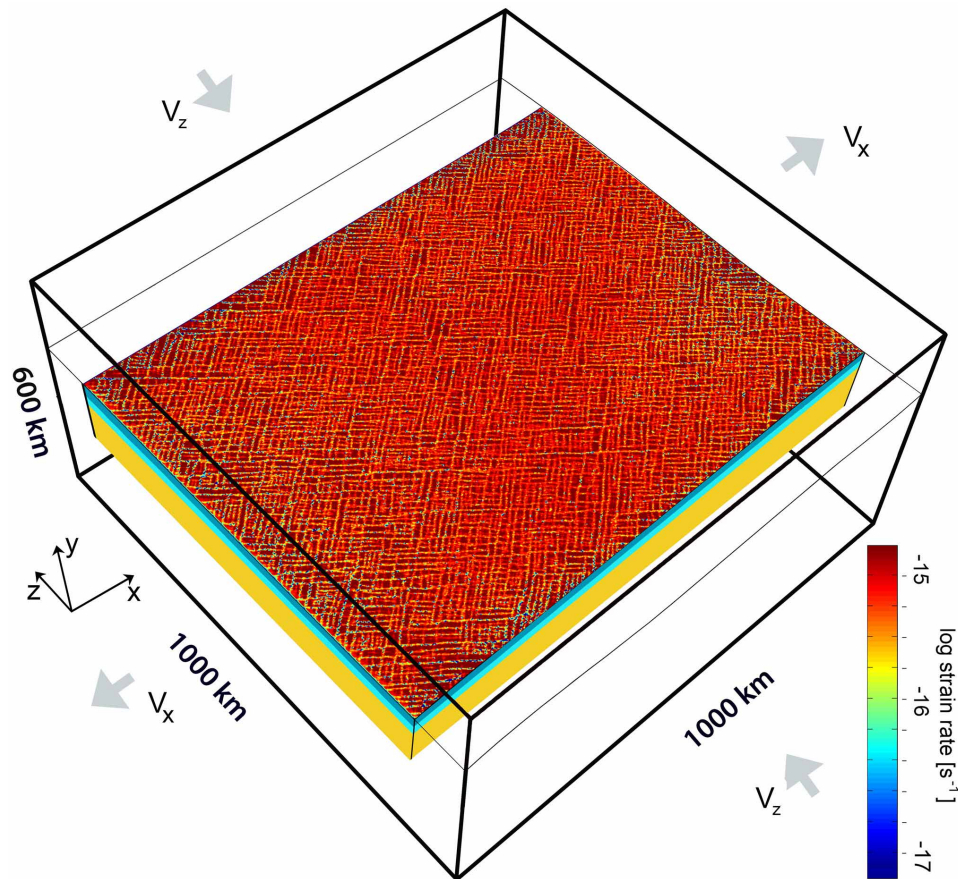
Surface topography

Moho topography



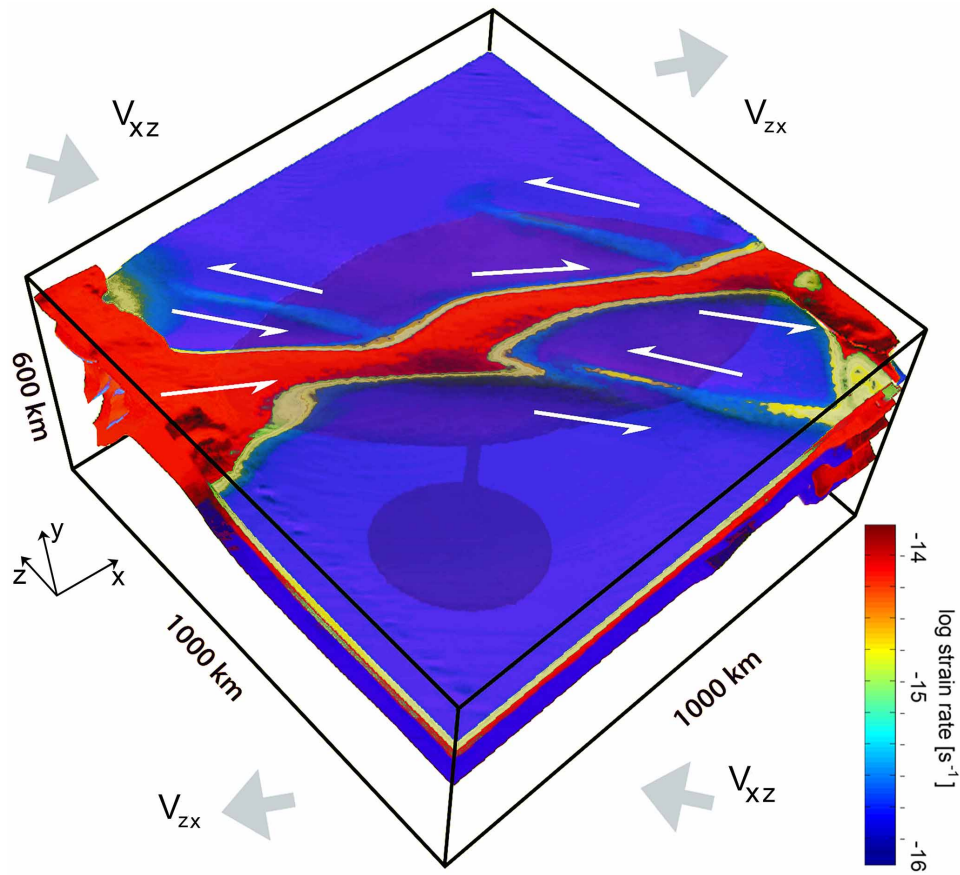
Extended Data Figure 6 | Stages of surface topography and Moho topography evolution in the case of the 3D experiment shown in Fig. 3. The left column ('topo') shows surface topography evolution, and the right column ('moho') shows the Moho topography evolution, with time increasing from top

to bottom. The experiment of Fig. 3 considers plume impingement on a lithosphere with a thermo-tectonic age of 250 Myr experiencing ultra-slow far-field extension at $V_x = 3 \text{ mm yr}^{-1}$. Note the large difference between the surface and Moho topography and wavelengths.



Extended Data Figure 7 | Ultra-high-resolution 3D experiment (grid cell size $2 \times 2 \times 2$ km, spatial grid dimensions $1,000 \times 1,000 \times 600$ km). Shown is surface evolution in the absence of a plume, in the case of bi-directional horizontal boundary conditions representing a combination of extensional and compressional pure shear far-field forcing (lateral velocities V_x , V_z of

respectively $+3 \text{ mm yr}^{-1}$ and -3 mm yr^{-1} applied on the pairs of opposite sides). In these settings, small-scale distributed conjugated fault patterns form at the surface (different to the distributed parallel linear faults observed in the case of uni-directional extension shown in Fig. 2).



Extended Data Figure 8 | 3D surface evolution in the case of plume–lithosphere interactions with bi-directional boundary conditions representing a combination of simple and pure shear far-field forcing. Lateral velocities with oblique V_x, V_z components, 3 mm yr^{-1} . Dark-blue

shaded zone shows the plume geometry. The resulting surface topography resembles an early stage of a segmented spreading centre with a strong strike-slip component and Riedel shear (for example, the Dead Sea rift, the Gulf of Aden).

Extended Data Table 1 | Thermomechanical parameters and boundary conditions used in numerical experiments³⁸

| | | |
|--------------|--|---|
| Thermal : | Surface temperature | 0°C |
| | Temperature at the bottom of the thermal lithosphere | 1330°C |
| | Thermal conductivity of crust | $2.5 \text{ W} \cdot \text{m}^{-1} \cdot ^\circ\text{C}$ |
| | Thermal conductivity of mantle | $3.5 \text{ W} \cdot \text{m}^{-1} \cdot ^\circ\text{C}$ |
| | Thermal diffusivity of mantle | $10^{-6} \text{ m}^2 \cdot \text{s}^{-1} \cdot ^\circ\text{C}$ |
| | Radiogenic heat production at surface | $1 \times 10^{-9} \text{ W} \cdot \text{kg}^{-1}$ |
| | Radiogenic heat production decay length | 10 km |
| | Thermo-tectonic age of the lithosphere, reference | 250Ma |
| | Thermo-tectonic age range of the lithosphere | 60-450 Ma |
| | Surface heat flow | 40- 60 $\text{mW} \cdot \text{m}^{-2}$ |
| | Mantle heat flow | 25-30 $\text{mW} \cdot \text{m}^{-2}$ |
| Mechanical : | Density for all materials | $\rho = f(P, T) (\text{kg} \cdot \text{m}^{-3})$ based on Perple_X ³³ |
| | Lamé elastic constants λ_e , G_e (here, $\lambda_e = G_e$) (N.B. in Flamar-based models only) | 30 GPa |
| | Plasticity, Byerlee's law – Friction angle, ϕ | 30° |
| | Plasticity, Byerlee's law – Cohesion, C | 20 MPa |
| | Plasticity, softening parameters ^{28,30} \tilde{N}_0, \tilde{N}_1 | 10 MPa, 3MPa |
| | Plasticity, softening parameters ^{28,30} $b_0, b_1, \varepsilon_0, \varepsilon_1$ | 0.6, 0., 0., 0.25 |
| | Plasticity, Peierls flow ($\tau_0, \dot{\varepsilon}, Q$) ³⁹ | 9100MPa, $1.3 \times 10^{-12} \text{ s}^{-1}$, 498 kJ mol^{-1} |

In mechanical parameters: Perple_X (ref. 33); softening parameters \tilde{N}_0, \tilde{N}_1 (refs 28, 30); softening parameters $b_0, b_1, \varepsilon_0, \varepsilon_1$ (refs 28, 30); Peierls flow $\tau_0, \dot{\varepsilon}, Q$ (ref. 39).

Extended Data Table 2 | Dislocation (A, n, E) and diffusion (A, n, E, a, m) ductile creep parameters used in this study

| Rock | Composition | A [MPa ⁻ⁿ s ⁻¹] | n | E [KJ·mol ⁻¹] | Reference |
|---|----------------------|---|-----|--------------------------------|-----------|
| Upper crust (continental) | wet westerly granite | 2×10^{-4} | 1.9 | 141 | 44 |
| Lower crust (continental) | Maryland diabase | 6.3×10^{-2} | 3.1 | 276 | 45 |
| Lower crust (continental) | Quartz-diorite | 3.2×10^{-2} | 2.4 | 212 | 46 |
| Mantle lithosphere (dislocation creep) | dry olivine | 1×10^4 | 3 | 510 | 39 |
| Mantle lithosphere | dry olivine | 1×10^4 | 3 | 510 | 39 |

We used 'classical' parameters most often used in convection and tectonic models. More recent data⁴⁰ predict slightly different values. However, in practice the impact of these differences is smaller than that of the uncertainties in the thermal and compositional structure of mantle and lithosphere⁴¹. The activation volume $V = 9.5 \times 10^{-6} \text{ m}^3 \text{ mol}^{-1}$ is taken into account for pressure dependence of viscosity in mantle materials⁴². For the diffusion creep (mantle), creep parameters are⁴³: activation energy $E = 300 \text{ kJ mol}^{-1}$, $A = 1.92 \times 10^{-10} \text{ MPa}^{-1} \text{ s}^{-1}$, $a = 1$, $m = 1$, $n = 1$. References: upper crust (continental) wet westerly granite⁴⁴, lower crust (continental) Maryland diabase⁴⁵, lower crust (continental) quartz-diorite⁴⁶, mantle lithosphere (dislocation creep) dry olivine³⁹, mantle lithosphere dry olivine³⁹.